# Dynamic wide gamut color generation using highly lossy metal-based metal-dielectric-metal structure

Yuusuke Takashima[1,2*], Kentaro Nagamatsu[1,2], Masanobu Haraguchi[1,2], and Yoshiki Naoi[1,2]

[1]Graduate School of Technology, Industrial and Social Science, Tokushima University, Tokushima 770-8506, Japan
[2]Institute of Post-LED Photonics, Tokushima University, Tokushima 770-8506, Japan

*E-mail: takashima@tokushima-u.ac.jp

Dynamic structural color control across a wide spectral range was experimentally achieved via phase retardation between orthogonal polarization states in a Ni/SiO$_2$/Ni-subwavelength grating (SWG) structure. The fabricated Ni/SiO$_2$/Ni-SWG structure exhibited spectrally broadened resonant reflection dips due to the optical damping of Ni. The resonances induced a large phase retardation between the p- and s-polarizations over a wide spectral range, and the retardation changed the reflected polarization states depending on the wavelength. The rotation of the analyzing polarizer enabled the dynamic variation of the reflected structural color from the sample across the wide visible color gamut.
© 2024 The Author(s). Published on behalf of The Japan Society of Applied Physics by IOP Publishing Ltd

Color generation is closely connected to our lives, and plays a significant role in several applications such as imaging, display, sensing, optical data storage, and security.[1,2] Light absorption by dyes and pigments is a standard coloration method. However, the coloration performance measured through operating wavelength, spectral purity, and lifetime, is restricted by the intrinsic physical properties and chemical instability of the dyes and pigments.

Structural color, which results from interactions between light and subwavelength structures, is a promising approach for controlling color and achieving high chemical stability.[2] This interaction provides resonant reflection, transmission, and absorption at specific wavelengths. The interaction conditions strongly depend on the structural parameters, and adjusting the structural dimensions enables artificial design of the resonant wavelength, efficiency, and spectral shape. Various types of structural colors have been reported for Fabry–Perot cavities,[3–5] metal-insulator-metal structures,[6,7] metal or dielectric gratings,[8–11] and Mie resonators.[12,13] Although these approaches achieve vivid colors with high spectral purity and chemical stability, only one static color is produced by each design unit. Additional fabrication of subwavelength structures is required to generate different colors.

Static color as well as multiple colors from a single design unit can be realized via dynamic control of the interaction between light and subwavelength structures. Many approaches for dynamic control of structural color were studied utilizing polarization states,[14,15] mechanical stretching,[16–18] phase-change materials,[19,20] metal-hydrides,[21] microfluid,[22] and electro-chemical depositions.[23] In particular, polarization-tunable structural colors are attractive for practical applications owing to their long lifetimes and fast response speeds.[24] To produce dynamic multicolors for different polarization states, several groups have employed anisotropic nanostructures, such as 1-dimensional gratings,[25–27] cross-shaped metal structures,[14,15] dielectric blocks,[28,29] and rectangular metal-insulator-metal structures.[30,31] However, dynamic wide spectral visible color generation from one design unit remains a challenge.

Herein, we experimentally achieved dynamic control of structural color across the wide visible spectrum using a highly lossy metal-based metal/insulator/metal-subwavelength grating (MIM-SWG) structure. In the general design of structural color, highly lossy materials are avoided because optical loss broadens the resonant spectral shape and degrades coloration performance. Our strategy combines spectrally broadened p- and s-polarization resonances to realize an ultrawide dynamic range. The fabricated lossy metal-based MIM-SWG structure showed spectrally broadened resonant reflection dips due to optical losses of the metal. The resonances also induce a large phase retardation between the p- and s-polarizations over a broad wavelength region, and the phase retardation varies the polarization states of the light reflected from the sample. Consequently, the measured reflection spectra of the sample could be controlled over the wide visible region by simply rotating the polarization of the light.

Figure 1(a) shows a schematic of the proposed MIM-SWG structure. The structure includes a thick, highly lossy metal, a transparent insulator film, and a highly lossy metal-based SWG. Ni was selected as the lossy metal because of its large optical dissipation in the visible wavelength region.[32] An SiO$_2$ film was used as the insulator material because of its high transparency.[33] The symbols, $\Lambda$, w, h$_{SWG}$, and t, represent the period, stripe width, SWG height, and insulator thickness, respectively. These structural parameters were optimized to obtain the deepest resonant reflection dip associated with the gap plasmon resonance between Ni and Ni-SWG (data not shown). The Ni/SiO$_2$/Ni-SWG structure was fabricated on an optical glass substrate using electron beam (EB) lithography and EB evaporation techniques. A 100 nm Ni film and a 70 nm SiO$_2$ film (t = 70 nm) were evaporated onto the glass substrate. An EB resist film (ZEP-520A, Zeon Co.) was spin-coated onto the evaporated SiO$_2$ spacer. The SWG pattern was drawn using an EB exposure system (ELS7500Y, Elionix Inc.), and the pattern was developed (ZED-50N, Zeon Co.). A 30 nm Ni film (h$_{SWG}$ = 30 nm) was evaporated onto the patterned EB resist and the resist was removed. Figure 1(b) shows the scanning electron microscopy (SEM) image of the top view of the fabricated sample after the resist removal. The measured structural parameters of the SWG were $\Lambda$ = 400 nm and w = 220 nm.
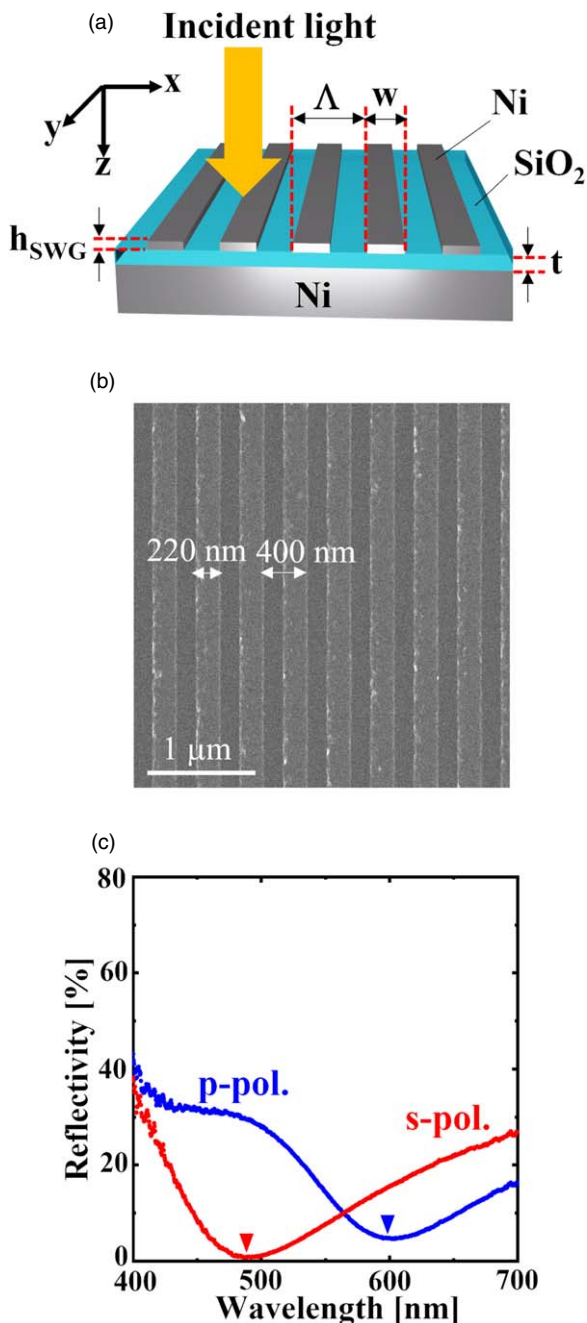
**Fig. 1.** (a) Schematic of the proposed Ni/SiO₂/Ni-SWG. (b) SEM image of the top view of the fabricated Ni/SiO₂/Ni-SWG. The scale bar is 1 $\mu$m. (c) The measured normal reflection spectra for s- (red) and p-polarized (blue) incidence.

We used a halogen lamp (LS-LHA, Sumita Co.) as a broadband visible light source to measure the reflection characteristics of the fabricated sample. The reflection spectra were measured using a spectrometer (FLAME-S, Ocean Insight Co.) and a microscope (BX53MTRF-S, Olympus Co.) with an objective lens (NA: 0.25, magnification: ×10). Figure 1(c) shows the measured normal reflection spectra for s- and p-polarized incidence (the electric fields of s- and p-polarization are parallel and perpendicular to the SWG stripes, respectively). For the reflection measurements, a commercialized broadband highly reflective mirror (TFMS-30C05-4/20, Shigmakoki Co.) was used as a reference. We obtained a relatively broad resonant dip in the p-polarized reflectivity at a wavelength of

approximately 600 nm. For s-polarization, the reflection was highly suppressed at a wavelength of approximately 490 nm.

To generate multiple colors dynamically from the fabricated sample, we placed two polarizers (U-AN360-3 and U-PO3, Olympus Co.) on the incident and reflected sides, as shown in Fig. 2. The angle of the input polarizer was fixed at $\theta_1 = 45°$. The reflection spectra were measured while rotating angle $\theta_2$ of the output polarizer. Figures 3(a)–3(h) show the measured reflection spectra as a function of $\theta_2$ ($\theta_1$ was fixed at 45°). The insets of Figs. 3(a)–3(h) show the corresponding optical images obtained using a CCD camera (DP22, Olympus Co.), and the squares indicate the 300 $\mu$m × 300 $\mu$m SWG region (note that these images were captured under halogen lamp illumination). At $\theta_2 = 0°$ and 90°, we obtained reflection spectra similar to those of the s- and p-polarizations, respectively [See Fig. 1(c)]. The satellite peaks in the spectra are attributed to the interference effect between the input and output polarizers. For $\theta_2$ values other than 0° and 90°, the fabricated sample distinctly showed different spectra from those of the p-and s-polarizations and the average of both polarizations. In particular, a green spectrum appears in the SWG region, even when the input and output polarizers are orthogonally related ($\theta_1 = 45°$, $\theta_2 = 135°$). Figure 4 shows a plot of the experimental reflection spectra in the CIE1931 color space using the CIE standard illuminant D65 and a 2° observer color-matching function (in this plot, we used these functions in the wavelength range from 400 to 700 nm in steps of 5 nm). The dashed lines show the sRGB region. By rotating the angle of the output polarizer from $\theta_2 = 0°$ to 180°, the reflection spectra of the fabricated structure became oval in the CIE1931 color space and covered the wide visible wavelength region. Thus, we experimentally realized an ultrawide range of dynamic colors from one design unit structure.

To discuss the origin of our dynamic wide gamut color generation, we calculated the electromagnetic field distribution using a commercial finite-difference time-domain (FDTD) solver (Poynting for Optics, Fujitsu Co.). We used the refractive indices of Ni and SiO₂ obtained from previous reports.[32,33] Figure 5(a) shows the numerically calculated
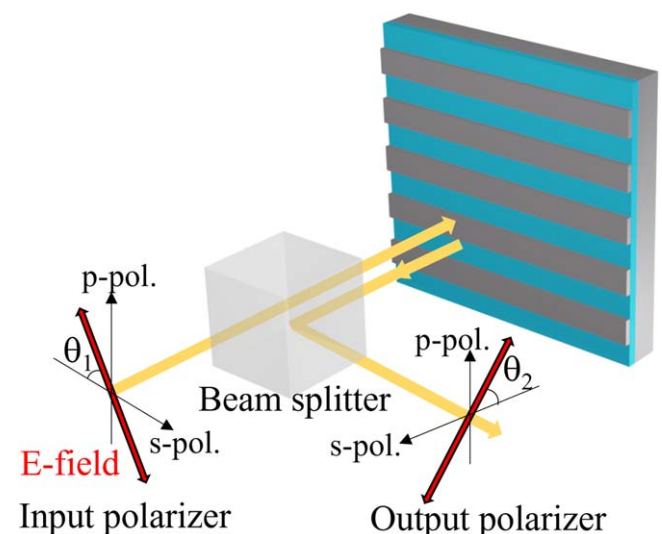


**Fig. 2.** Measurement setup for dynamic color generation from the fabricated Ni/SiO₂/Ni-SWG. The symbols $\theta_1$ and $\theta_2$ indicate the polarization angles of the input and output polarizers, respectively.
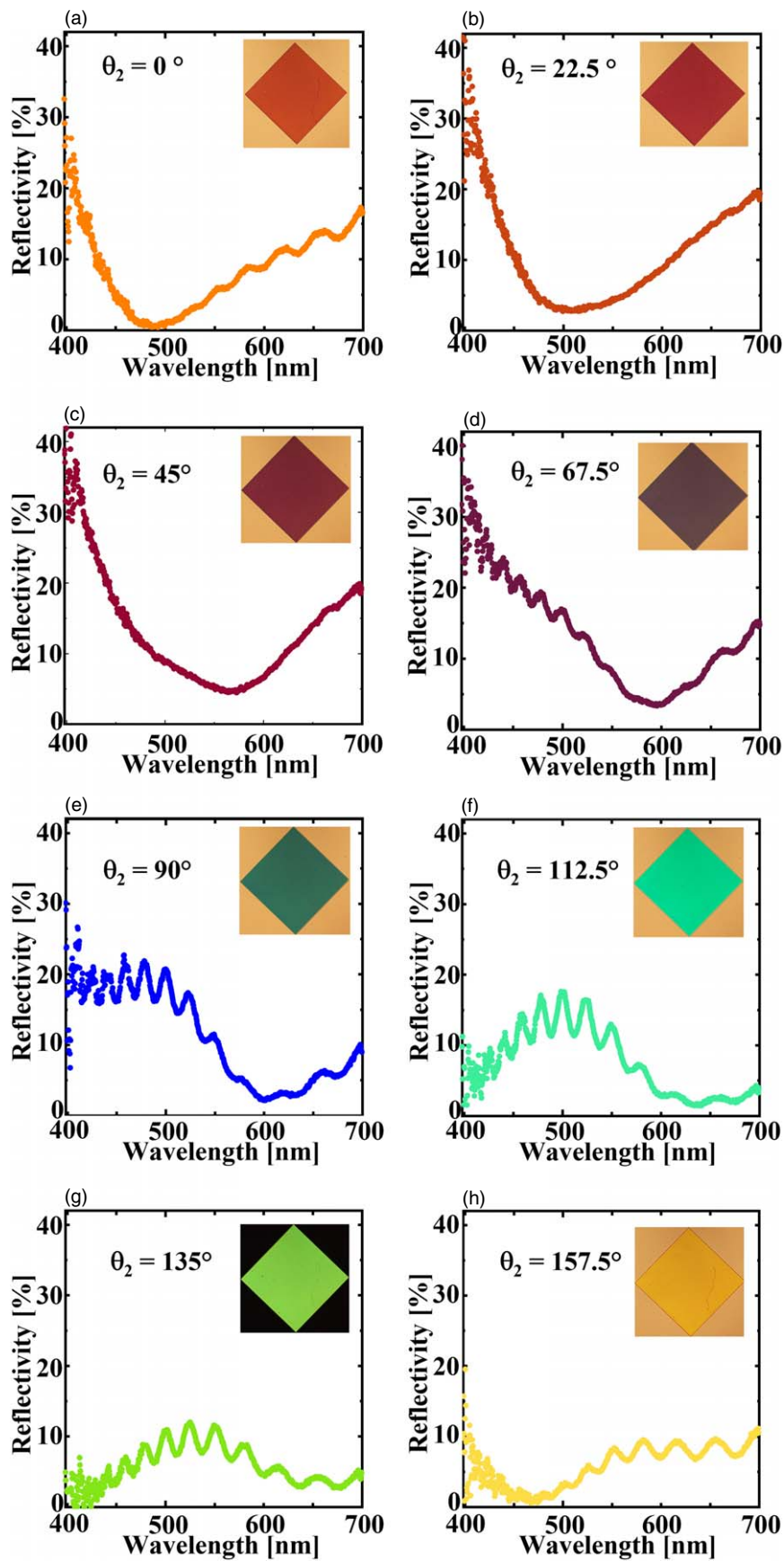
**Fig. 3.** (a)–(h). Measured reflection spectra of the fabricated Ni/SiO$_2$/Ni-SWG structure at various $\theta_2$ values ($\theta_1$ is fixed at 45°). The insets show the corresponding optical images captured using a CCD camera. The square regions in the insets show the 300 $\mu$m × 300 $\mu$m SWG.
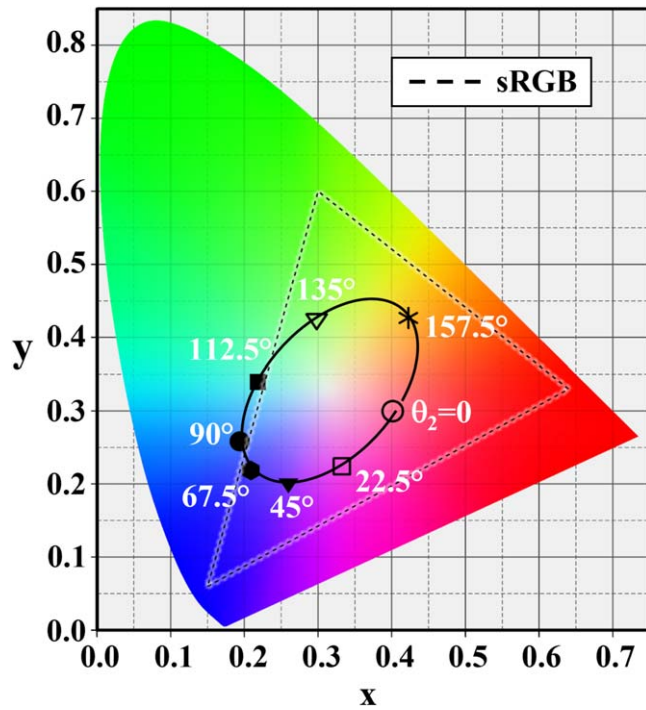
**Fig. 4.** CIE1931 chromaticity coordinate plot of the measured reflection spectra from the Ni/SiO₂/Ni-SWG structure. The plots used CIE illuminant D65 and CIE1931 2° observer color-matching function. The dashed lines show the sRGB space.

p- and s-polarization reflection spectra and the phase differ-ence $\varphi_p - \varphi_s$ between the two polarizations, where $\varphi_p$ and $\varphi_s$ are the phases of the reflected light for p- and s-polarizations, respectively. The calculated reflection spectra of p- and s-polarizations show reflection dips at wavelengths of 570 and 420 nm, respectively. The tendencies of the calculated p- and s-polarization spectra coincide with the experimental spectra.

Figures 5(b) and 5(c) show the calculated electric field distributions for p- and s-polarizations at each resonant wavelength, respectively. Although the incident light propagates along the z-direction [the coordinates are shown in Fig. 1(a)], Fig. 5(b) indicates that a localized z-component of the electric field ($E_z$) for p-polarization appears between the SWG and the metal substrate. This distribution agrees well with the typical gap plasmon and magnetic dipole modes in previous studies.[1,6,7] This distribution indicates that the MIM-SWG structure strongly confines light to the SiO₂ film and highly suppresses reflection. However, the field localization into the SiO₂ film for s-polarization is not observed [Fig. 5(c)]. The electric field of s-polarization is distributed in the air gap between the Ni-SWG stripes. This distribution indicates that the reflection dip of s-polarization mainly results from destructive interference (namely, anti-reflection condition) at the bottom Ni/SiO₂ and SiO₂/air interfaces.

Figure 5(a) shows the phase difference between the p- and s-polarizations. An abrupt change in the phase difference appears near the reflection dip wavelengths. A broad phase difference spectrum is obtained in the wide wavelength region from 435 to 555 nm. The shape of this phase spectrum deviates significantly from that of low-loss metals such as Ag-based plasmonic structure.[26]
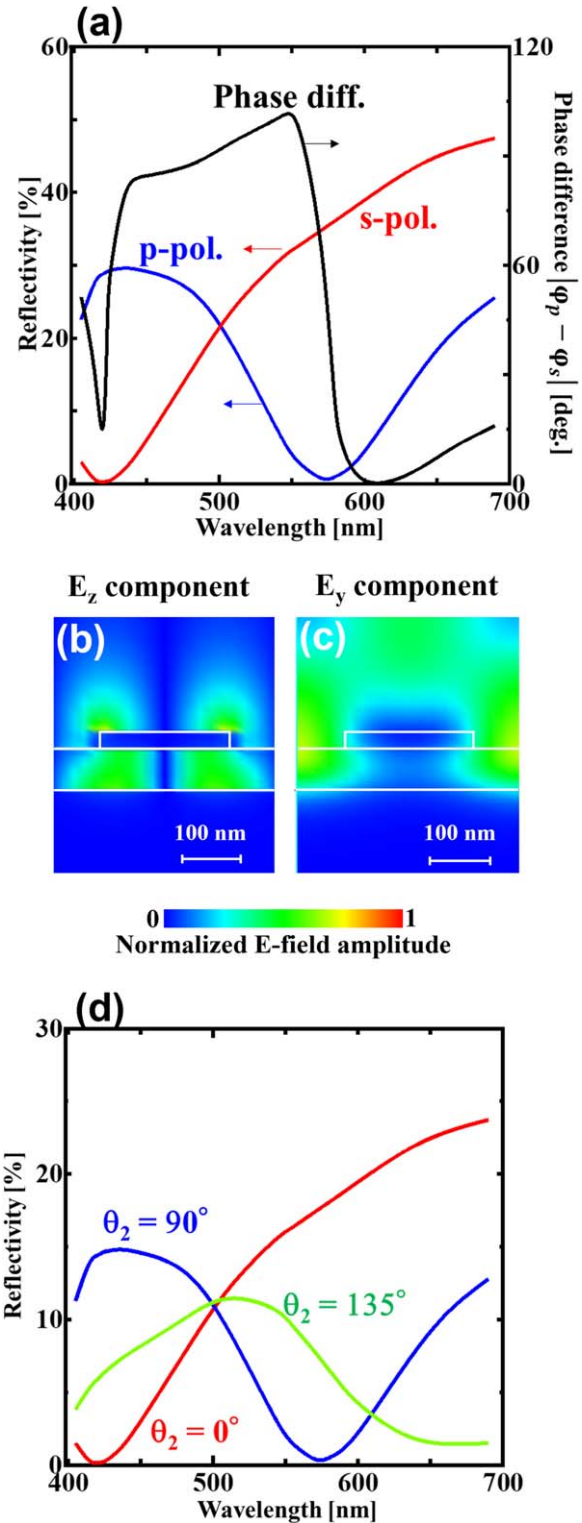




**Fig. 5.** (a) Calculated s- (red) and p-polarization (blue) reflection spectra of the fabricated Ni/SiO₂/Ni-SWG structure. The black curve shows the phase difference between the two orthogonal polarizations. (b) z-component electric field distribution ($E_z$) for p-polarization at resonant wavelength. (c) y-component electric field distribution ($E_y$) for s-polarization at resonant wavelength. (d) Calculated reflection spectra at output polarization angle $\theta_2 = 0$, 90, and 135°.

The experimental reflection characteristics of the fabricated sample were analyzed using Jones matrices containing polarization state and phase information. Equation (1) gives the normalized electric field $E_r(\theta_1, \theta_2)$ of the light reflected through the input and output polarizers.[25]

$$E_r(\theta_1, \ \theta_2)$$

$$= \begin{bmatrix} \cos^2\theta_2 & \sin\theta_2\cos\theta_2 \\ \sin\theta_2\cos\theta_2 & \sin^2\theta_2 \end{bmatrix} \begin{bmatrix} \sqrt{R_s}\,e^{i\varphi_s} & 0 \\ 0 & \sqrt{R_p}\,e^{i\varphi_p} \end{bmatrix} \begin{bmatrix} \cos\theta_1 \\ \sin\theta_1 \end{bmatrix}$$

$$(1)$$

where $R_p$ and $R_s$ are the calculated reflectivities of the MIM-SWG structure for the p- and s-polarizations, respectively. To clarify the dependence of the reflection spectra on the polarization states, we calculated $|E_r(\theta_1, \theta_2)|^2$ based on Eq. (1), because the reflected light intensity is proportional to the square of the electric field amplitude. The calculated reflection spectra at output polarizer angles $\theta_2 = 0°$, 90°, and 135°, are shown in Fig. 5(d) ($\theta_1$ was fixed at 45°). We obtained the s- and p-polarization reflection spectra at $\theta_2 = 0°$ and 90°. The reflection green spectrum appeared with an orthogonal alignment between the input and output polarizers ($\theta_2 = 135°$) because the resonant dips and phase difference vary the polarization state of the reflected light. Compared with previous reports, our sample covers the wider dynamic range in CIE1931 color gamut.[28,30] These results suggest that spectrally broadened resonant reflection dips and flat phase difference spectra are important for dynamic wide gamut color generation. The calculated spectra can describe the experimental characteristics. On the other hand, the resonant wavelengths in calculation are differ from these in the experiment [Figs. 5(d) and 3(a), 3(e), 3(g)]. The difference between the experimental and calculated spectra can be attributed to the following two reasons. (i) The focusing incidence. The focused light in the experimental measurements contains not only the normal-incidence component but also the oblique component, whereas the calculation is based on normal incidence. This is very important for practical applications, and the investigation for the oblique incidence will be reported in elsewhere. (ii) The refractive index difference between the evaporated films (Ni and $SiO_2$) and these in the calculation. Especially, the refractive index deviation of $SiO_2$ has a large influence on the resonant wavelength because the gap plasmon resonance strongly depends on the optical thickness of the spacer between metals.

In conclusion, we experimentally demonstrated dynamic wide gamut color generation using a highly lossy metal-based MIM-SWG structure. The fabricated Ni/$SiO_2$/Ni-SWG structure exhibited resonances resulting from the gap plasmon and destructive interference for the p- and s-polarizations. These resonances provide spectrally broadened dips in the reflection spectra and the phase difference between the orthogonal polarization states. The fabricated sample exhibited an ultrawide oval shape in the CIE1931 color space by simply rotating the polarization. Our calculations showed that resonance-induced reflection dips and phase difference are important for wide dynamic range of color generation. Our strategy of using a highly lossy material had a significant impact on the design of dynamic coloration. In further work, we plan to demonstrate more precise and wider color control using the various polarization angle including 45°.

1) S. Daqiqeh Rezaei, Z. Dong, J. You En Chan, J. Trisno, R. J.-H. Ng, Q. Ruan, C. W. Qiu, N. A. Mortensen, and J. K.-W. Yang, ACS Photonics **8**, 18 (2021).
2) D. Wang, Z. Liu, H. Wang, M. Li, L. J. Guo, and C. Zhang, Nanophotonics **12**, 1019 (2023).
3) Z. Li, S. Butun, and K. Aydin, ACS Photonics **2**, 183 (2015).
4) K. Lee, S. Han, Z. Li, H. Baac, and H. Park, Sci. Rep. **9**, 14917 (2019).
5) Z. Yang, C. Ji, D. Liu, and L. Guo, Adv. Optical Mater. **7**, 1900739 (2019).
6) M. Miyata, H. Hatada, and J. Takahara, Nano Lett. **16**, 3166 (2016).
7) S. D. Rezaei, R. J. Hong Ng, Z. Dong, J. Ho, E. H.-H. Koay, S. Ramakrishna, and J. K.-W. Yang, ACS Nano **13**, 3580 (2019).
8) D. B. Mazulquim, K. J. Lee, J. W. Yoon, L. V. Muniz, B.-H. V. Borges, L. G. Neto, and R. Magnusson, Opt. Express **22**, 30843 (2014).
9) Y. Horie et al., Nano Lett. **17**, 3159 (2017).
10) Y. Kim, K. Jung, J. Cho, and J. Hyun, ACS Nano **13**, 10717 (2019).
11) Y. Takashima, M. Haraguchi, and Y. Naoi, Opt. Mater. Express **11**, 2712 (2021).
12) Y. Nagasaki, M. Suzuki, I. Hotta, and J. Takahara, ACS Photonics **5**, 1460 (2018).
13) W. Yang, S. Xiao, Q. Song, Y. Liu, Y. Wu, S. Wang, J. Yu, J. Han, and D.-P. Tsai, Nat. Commun. **11**, 1864 (2020).
14) T. Ellenbogen, K. Seo, and K. Crozier, Nano Lett. **12**, 1026 (2012).
15) Z. Li, A. Clark, and J. Cooper, ACS Nano **10**, 492 (2016).
16) L. Zhu, J. Kapraun, J. Ferrara, and C. J. Chang-Hasnain, Optica **2**, 255 (2015).
17) H. Honma, K. Takahashi, M. Ishida, and K. Sawada, Appl. Phys. Express **9**, 027201 (2016).
18) A. L. Holsteen, A. F. Cihan, and M. L. Brongersma, Science **365**, 257 (2019).
19) F. Shu, F. Yu, R. Peng, Y. Zhu, B. Xiong, R. Fan, Z. Wang, Y. Liu, and M. Wang, Adv. Opt. Mater. **6**, 1700939 (2018).
20) Q. He, N. Youngblood, Z. Cheng, X. Miao, and H. Bhaskaran, Opt. Express **28**, 39841 (2020).
21) X. Duan, S. Kamin, and N. Liu, Nat. Commun. **8**, 14606 (2017).
22) S. Sun, W. Yang, C. Zhang, J. Jing, Y. Gao, X. Yu, Q. Song, and S. Xiao, ACS Nano **12**, 2151 (2018).
23) C. Moon, Y. Kim, and J. Hyun, Nat. Commun. **13**, 3391 (2022).
24) F. Neubrech, X. Duan, and N. Liu, Sci. Adv. **6**, eabc2709 (2020).
25) L. Duempelmann, A. Luu-Dinh, B. Gallinet, and L. Novotny, ACS Photonics **3**, 190 (2016).
26) M. Song, X. Li, M. Pu, Y. Guo, K. Liu, H. Yu, X. Ma, and X. Luo, Nanophotonics **7**, 323 (2018).
27) Y. Jung, H. Jung, H. Choi, and H. Lee, Nano Lett. **20**, 6344 (2020).
28) X. Shang, J. Niu, H. Li, L. Li, H. Hu, C. Lu, and L. Shi, Photonics **10**, 448 (2023).
29) L. Wang, T. Wang, R. Yan, X. Yue, H. Wang, Y. Wang, J. Zhang, X. Yuan, J. Zeng, and J. Wang, Nano Lett. **23**, 5581 (2023).
30) M. Kim, I. Kim, J. Jang, D. Lee, K. T. Nam, and J. Rho, Appl. Sci. **8**, 982 (2018).
31) H.-C. Wang and O. J.-F. Martin, Adv. Opt. Mater. **11**, 2202165 (2023).
32) P. B. Johnson and R. W. Christy, Phys. Rev. B **9**, 5056 (1974).
33) L. Gao, F. Lemarchand, and M. Lequime, J. Eur. Opt. Soc. Rapid Publ. **8**, 13010 (2013).